The Relevance of High-frequency Analysis Artifacts to Remote Triggering

Zhigang Peng,[1] Leland Timothy Long,[1] and Peng Zhao[1,2]

Online material: Six supplemental figures

INTRODUCTION

The high-frequency content observed in teleseisms recorded by seismometers can be produced either by the nonlinear behavior of seismometers and digitizers (Delorey *et al.* 2008; Hellweg *et al.* 2008) or by the real Earth response. The latter include scattering from small-scale heterogeneities during seismic wave propagation (*e.g.*, Chen and Long 2000) and high-frequency radiations from the earthquake source (*e.g.*, Peng *et al.* 2006) or near-surface regions near the recording site (Fischer *et al.* 2008). Recent studies have shown that large-amplitude surface waves generated by earthquakes at regional and teleseismic distances could also trigger high-frequency seismic sources, either in the form of regular earthquakes at seismogenic depth near the recording site (Hill and Prejean 2007 and references therein) or "non-volcanic" tremor in the lower crust (Rubinstein *et al.* 2010; Peng and Gomberg 2010 and references therein).

In teleseisms the presence of high-frequency content (*e.g.*, >5 Hz) in the seismogram is inconsistent with the expected attenuation of waves from a distant source (*i.e.*, >1,000 km). The lack of frequencies above 5 Hz in a teleseism makes it easy to separate the seismic signals of locally triggered events from those of the teleseism by applying a high-pass or band-pass filter to broadband continuous recordings (*e.g.*, Hill and Prejean 2007; Velasco *et al.* 2008). Another effective way to demonstrate triggered seismicity is the spectrogram display (*i.e.*, frequency-time plot) of the seismic data (*e.g.*, West *et al.* 2005; Hill and Prejean 2007; Peng and Chao 2008; Peng *et al.* 2008). In such a plot, the locally triggered seismic signals typically show as narrow vertical bands rich in high-frequency energy within the low-frequency body and/or surface waves of teleseismic events.

When examining high-frequency signals for evidence of remote triggering, it is important to distinguish between genuine high-frequency signals from triggered events and those from seismic instruments or analysis procedures. For example, Hellweg *et al.* (2008) found that due to digitization errors,

large long-period surface waves of the 2002 *Mw* 7.8 Denali fault earthquake recorded at the STS-1 broadband sensors in northern California produced high-frequency noises that mimic the pattern of remotely triggered tremor and earthquakes. In this article we show that signal processing artifacts could also introduce high-frequency energy in the spectrogram plot that mimics remote triggering of earthquakes and/or tremor. In the following section, we first describe the general observation, followed by a detailed explanation. Next, we offer several procedures to correct for such artifacts, and discuss our results in the context of previous observations.
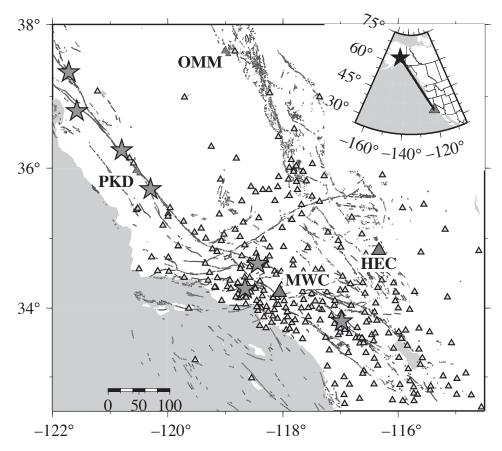
OBSERVATIONS

In an effort (Fabian *et al.* 2009) to identify additional triggered tremor in southern California (Figure 1), spectrograms were computed from all the seismic records in the Southern California Earthquake Data Center (SCEDC) that recorded the 2002 *Mw* 7.8 Denali fault earthquake (Figure 1). This event was chosen because it triggered many microearthquakes (*e.g.*, Prejean *et al.* 2004) and tremor (Rubinstein *et al.* 2007; Gomberg *et al.* 2008; Peng *et al.* 2008, 2009) in western Canada and the United States. In particular, Gomberg *et al.* (2008) conducted a systematic survey of tremor in California, and identified at least seven places along the San Andreas fault system that have generated clear tremor signals.

We use the command "*specgram*" in MATLAB to generate spectrograms with the following parameters: *specgram(a,nfft,fs,window,noverlap)*, where *a* is the data, *nfft* is the number of points used to calculate the discrete fast Fourier transform (FFT), *fs* is the sampling rate, *window* is a periodic Hanning window, and *noverlap* is the number of samples by which two consecutive sections overlap. In this study, we use *nfft* = 256, *window* = *nfft*, and *noverlap* = *window* x 0.75 = 192. For the sampling rate *fs* =100/s, the window length is 2.56 s. These parameters are either the default or typical values used in computing the spectrogram. We have set those parameters to different values (*nfft* from 64 to 512, and *noverlap* from 50 to 250), and the results are generally similar to those shown below. We also use another MATLAB command *spectrogram(a, window, noverlap, nfft, fs)* with the same values. The main difference is that the "*specgram*" command uses the Hanning window,

1. School of Earth and Atmospheric Sciences, Georgia Institute of Technology, Atlanta, Georgia, U.S.A.
2. NORSAR, Kjeller, Norway

▲ **Figure 1.** A map view of the study region in central and southern California. The dark lines denote surface traces of active faults. Seismic stations from the Southern California Seismic Network (SCSN with the network ID CI) are denoted with gray triangles. The broadband stations MWC, HEC, PKD (belonging to the Berkeley Digital Seismic Network with the network ID BK), and OMM (belonging to the Northern Nevada Seismic Network with the network ID NN) are shown as solid triangles. The gray stars mark the locations of tremor triggered by the 2002 *Mw* 7.8 Denali fault earthquake (Gomberg *et al.* 2008). The inset shows the epicenter of the 2002 *Mw* 7.8 Denali fault earthquake (star), the station PKD (triangle), and the great circle ray path.
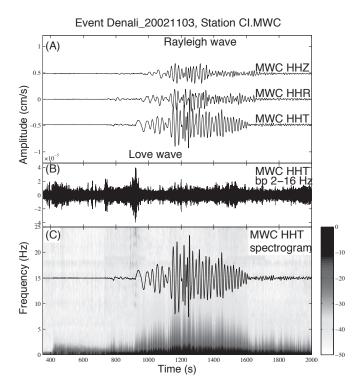
while the "*spectrogram*" command uses the Hamming window. Because the Hanning window does a better job of reducing high frequencies beyond the first lobe, the spectrogram plots shown below are all generated by the "*specgram*" command. Further reference can be found in the MATLAB code documentation for both commands.

Figure 2 shows an example of the original three-component broadband seismograms (HH channels), 2–16 Hz bandpass-filtered transverse component, and the corresponding spectrogram recorded by station MWC on San Gabriel Mountain. A general pattern in the spectrogram from this and other stations equipped with broadband seismometer/digitizer systems (Ⓔ see Figure S1, available in the electronic supplement to this paper) is bursts of high-frequency energy during the large-amplitude surface waves. A zoom-in plot (Ⓔ see Figure S2, available in the electronic supplement to this paper) reveals that the high-frequency energy is mostly centered on the zero crossing in the broadband seismograms. In comparison, the spectrogram from the short-period recordings (EH channel) at the same station does not show elevated high-frequency energy during the long-period surface waves (Ⓔ see Figure S3, available in the electronic supplement to this paper). We also note

that the high-frequency signal is only shown in the spectrogram plot, and not in the 2–16 Hz bandpass-filtered seismograms (Figure 2B and Ⓔ Figure S1B, available in the electronic supplement to this paper). Finally, previous studies have found that the period of the triggered high-frequency burst should approximate one cycle of the surface waves (*e.g.*, Peng *et al.* 2008, 2009; Hill 2008, 2010; Gonzalez-Huizar and Velasco 2011), not the half-cycle pattern as observed in Ⓔ Figure S2 (available in the electronic supplement to this paper). These lines of evidence suggest that the high-frequency energy in the spectrogram is likely caused by a processing artifact, rather than true seismic signals originated from the subsurface.

SYNTHETIC EXAMPLES

To further support the above hypothesis, we generate a synthetic seismogram from a pure sine function with 20-s period that mimics the typical 20-s surface waves with the same sampling rate (100/s). Then we use the "*specgram*" command in MATLAB and the same parameters to compute the spectrogram of the synthetic seismogram (Figure 3). Ideally the spectrogram should only show energy concentrated at 20 s, which
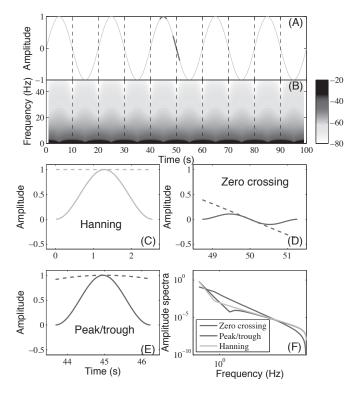
▲ Figure 2. A) Instrument-correlated three-component seismograms generated by the 2002 *Mw* 7.8 Denali fault earthquake and recorded at the broadband station CI.MWC in southern California. B) 2–16 Hz bandpass-filtered transverse-component seismogram showing locally generated high-frequency signals. C) The spectrogram of the transverse-component seismogram at station CI.MWC shaded by the amplitude in db below the maximum. The original transverse-component seismogram is plotted at 15 Hz for comparison.

would be close to bottom of the *y*-axis (0 Hz) if the frequency scale is linear. The spectrogram plot, however, shows elevated high-frequency energy that is centered on the zero crossing of sine function, similar to the observations from the real data (*e.g.*, Figure 2). These results demonstrate that the high-frequency energy shown in the spectrogram is probably caused by the analysis procedure.

Next, we cut the data around the zero crossing and the peak/trough of the synthetic seismogram, apply the Hanning window, and then compute the FFT. Figure 3F shows that the spectrum of the windowed data around the peak/trough matches that of a pure Hanning window for frequencies larger than 3 Hz. The high-frequency energy for the Hamming window is higher than for the Hanning window (Ⓔ see Figure S4, available in the electronic supplement to this paper), and the observed correlation (energy peak at zero crossing and energy hole at peak/trough) is more prominent.
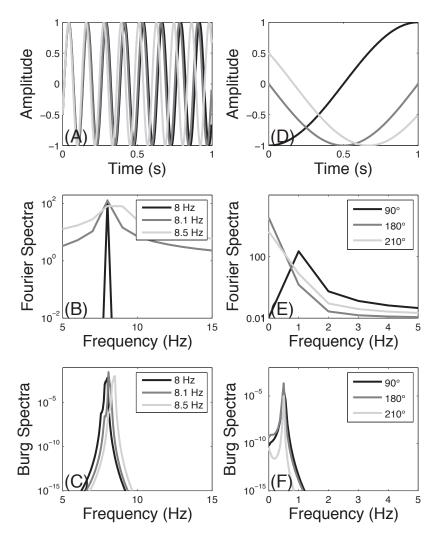
EXPLANATION

In this section we briefly explain the underlying cause of the high-frequency artifact in both the synthetic and real observations. The spectrogram shown before is computed from

▲ Figure 3. A) A sine function with a period of 20 s. A Hanning window is applied to the segments marked with light gray (zero crossing) and black (peak/trough) respectively. The resulting time series after the Hanning window are shown in (D) and (E), and the corresponding spectra are shown in (F). The vertical dashed lines mark the zero crossing. B) The spectrogram computed using the "*specgram*" command in MATLAB. The corresponding input parameters are given in the main text. C) The Hanning window (solid) and data with amplitude = 1 (dashed). D) The truncated data around zero crossing (dashed) and after applying the Hanning window (solid). E) The truncated data around the peak/trough (dashed) and after applying the Hanning window (solid). F) The Fourier spectra of the Hanning window (light gray), the windowed zero crossing (gray), and windowed peak/trough (black).

discrete-time Fourier transform of a signal using a sliding window of a finite length. Ideally, the pure sine wave is an impulse or spike in the frequency domain. When a window of finite length is applied in the time domain, it corresponds to the convolution of the spectrum of the window with the spike in the frequency domain. In the case of a simple box car window, the corresponding spectrum is a $\text{sinc}(x) = \sin(x)/x$ function. Mathematically, the FFT treats the windowed trace as circular, with the end of the trace continuing at the beginning of the trace. Frequency components that are exact multiples within the truncated signal have components that fall on the zeros of $\sin(x)/x$. Any frequency component that is not a multiple within the sample increment falls off the zeros of $\sin(x)/x$ and introduces high-frequency energy into the resulting spectrum (Figure 4B). In addition, data with spectral-component periods longer than the sample window cannot be well resolved (Figure 4E), and hence they are particularly susceptible to introducing
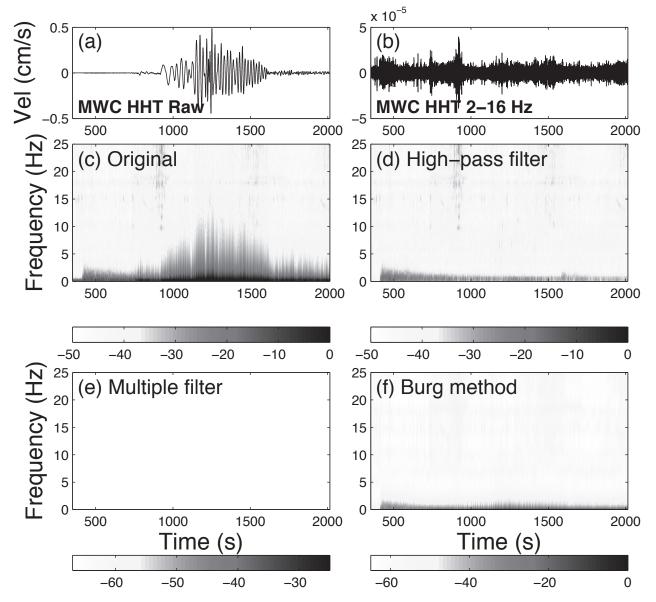
▲ **Figure 4.** A) Three sine functions with the same phase (30°) and slightly different frequencies. B) The Fourier spectra of the sine functions shown in (A). C) The Burg spectra of the sine functions shown in (A). We use the MATLAB command *pburg*(*x,p,nfft,fs*) with *p* = 30 and *nfft* = 4,096. See texts for detailed description of each parameter. D) Three sine functions with the same frequency (0.5 Hz) and different phases. E) The Fourier spectra of the sine functions shown in (D). F) The Burg spectra of the sine functions shown in (D).

high-frequency artifacts into the filtered signal, especially near the zero crossing when the discontinuity between the start and end of the window is large (Figure 4E). The Hanning and Hamming windows are designed to minimize this effect, while the Hanning window produces less high-frequency spectral artifact than the Hamming window (Ⓔ see Figure S4, available in the electronic supplement to this paper). However, it is not possible to completely eliminate high-frequency contamination with any window. When the amplitude of the signal is large (*e.g.*, during large-amplitude surface waves), the windowing effect is amplified, resulting in the high-frequency artifact in the spectrogram plot.

CORRECTION

After identifying the cause of the artificial high-frequency energy in the spectrogram during the long-period surface waves, we propose the following procedures to reduce this artifact. One simple way is to apply a high-pass filter to the

entire trace to remove those long-period signals that cannot be resolved by the short time window before computing the spectrogram. Figure 5D shows the spectrogram plot from the transverse-component broadband data at station MWC after applying a two-pass fourth-order 0.5 Hz high-pass filter. We use the "*specgram*" command and the same parameters to compute the spectrogram. We choose 0.5 Hz because the corresponding period (2 s) is close to the 2.56 s window length. As compared with Figure 5C (which is the same as Figure 2C), the high-frequency energy is greatly reduced in the updated spectrogram plot. In addition, the updated spectrogram is consistent with that from the short-period recordings (Ⓔ see Figure S3, available in the electronic supplement to this paper) and the 2–16 Hz bandpass-filtered data (Figure 2B), again suggesting that the aforementioned artifact is largely reduced. One drawback of this procedure is that the energy from the long-period surface wave is lost. However, this is still tolerable if the main purpose is to demonstrate potential triggered seismicity that is rich in the high-frequency bands (*e.g.*, Hill and Prejean 2007).

▲ Figure 5. A comparison of the spectrogram for the transverse-component data at the broadband station CI.MWC with and without corrections. (A) Instrument-correlated transverse-component seismogram generated by the 2002 Mw7.8 Denali Fault earthquake and recorded at CI.MWC. (B) 2-16 Hz band-pass-filtered transverse-component seismogram. (C) The spectrogram without correction. (D) The spectrogram after applying the 0.5 Hz high-pass-filter to the data. (E) The spectrogram computed from the multiple band-pass-filter technique. (F) The spectrogram from the Burg method. See text for details of the parameters employed in each procedure.

The second procedure involves multiple bandpass filters. We directly generate narrow bandpass filtering of the raw seismograms using the built-in command "*bp*" in the seismic analysis code (SAC), and place them into a matrix so that it can be plotted as a spectrogram. We use a two-pass fourth-order Butterworth bandpass-filter with a bandwidth of 0.5 Hz, and slide from 1 to 40 Hz by every 0.25 Hz. Similar results are obtained if we choose slightly different parameters. As shown in Figure 5E, the artificial high-frequency energy during the large-amplitude surface waves at these stations disappears. In addition, the signals in the spectrogram plots correlate well with those in the 2–16 Hz bandpass-filtered seismograms (Figure 2B). Such improvement is not surprising, because we

did not introduce any short time windowing effects in the time axis, and the spectrogram is simply generated from the bandpass-filtered seismograms.

In the third procedure, we use the Burg method (Burg 1967) to estimate the spectrum at each moving-time window. The Burg method computes the spectrum by maximizing the entropy of a time series and is characterized by higher resolution in the frequency domain than traditional FFT spectral analysis, especially for a relative short time window (Buttkus 2000). The tradeoff is loss in precision in the amplitudes in the spectra. Specifically, the Burg method first considers the time series as an autoregressive (AR) process and calculates the coefficient of the process for a fixed order p (Andersen 1974). Then,

the FFT spectrum is estimated using the previously calculated AR coefficients with a sampling length *nfft* (Ulrych and Bishop 1975; Buttkus 2000). We use the MATLAB command *pburg(x,p,nfft,fs)* to compute the Burg spectrum, where *x* is samples of a discrete-time signal, *p* is the integer specifying the order of an autoregressive (AR) prediction model for the signal, *nfft* is the integer sampling length used to calculate the spectrum, and *fs* is the sampling frequency. In this study, we use the data window of 2.56 s with 75% overlap to compute the Burg spectrogram, which is the same in the "*spectrogram*" and "*specgram*" commands. We choose *p* = 30 as the order of AR models, which minimizes both the final prediction error (FPE) (Akaike 1970; Buttkus 2000) and the computation work. We use *nfft* = 4,096 as the sampling length, which provides a high resolution and reliable results in the frequency domain.

The resulting spectrogram from the Burg method for station MWC (Figure 5F) is similar to the first two procedures, yet the energy distribution is smoother, due to an increase of frequency resolution. In addition, the spectrogram's amplitude range is much wider due to the distortion of amplitudes in the Burg spectrum. We also see some spiky signals in the first few Hz during the large-amplitude surface waves. These spiky signals are generated by the same windowing effects as shown before, yet their spread is much less compared with the conventional FFT method with the Hanning window.

We use the same procedures to generate an updated spectrogram plot (Ⓔ see Figure S5, available in the electronic supplement to this paper) for the broadband seismograms recorded by station PKD near the Parkfield section of the San Andreas fault (Peng *et al.* 2008). The updated spectrograms correlate better with the 2–16 Hz bandpass-filtered data, suggesting that the artificial high-frequency signals caused by the windowing effects are largely suppressed with the updated procedures, while the genuine signals remain. Ⓔ Figure S6 (available in the electronic supplement to this paper) shows updated spectrogram plots for the triggered earthquakes recorded by the broadband station OMM near the Long Valley caldera in eastern California (Hill and Prejean 2007). The high-frequency signals in the range of 1–10 Hz track the amplitudes of the seismogram and are more elevated than those shown in Figure 6 of Hill and Prejean (2007). This difference is likely due to the choice of color range "*caxis*" when plotting the spectrogram (D. P. Hill, personal communication 2010). After correction, the artificial high-frequency signals are largely reduced (Ⓔ see Figures S6D–F, available in the electronic supplement to this paper), while the signals associated with the triggered earthquakes during the *S* waves and the Rayleigh waves become much clearer.

DISCUSSION

High-frequency signals in seismograms could be produced during all stages of seismic wave propagation (*i.e.*, source, path and site) and recording. In this short note, we pointed out another possible source of high-frequency signals in the spectrogram plot caused by the analysis procedure. When we computed the Fourier transform and the spectrogram, artificial high-frequency signals could be generated if the window length is shorter than the predominant periods of the input seismic waves. Such high-frequency signals show perfect correlations with the large-amplitude surface waves (Figure 2 and Ⓔ Figure S1, available in the electronic supplement to this paper), similar to the patterns of recently observed triggered earthquakes and tremor. However, such signals mostly correlate with the zero crossing of the long-period surface waves, which is inconsistent with the dynamic stress perturbations that are mostly associated with either peak or trough of surface waves with one full cycle. In addition, these signals only appear in the spectrograms of broadband recordings, not in the spectrograms of short-period recordings or bandpass-filtered seismograms, suggesting that they are generated when computing the spectrograms of broadband recordings.

Because the spectrogram plot has been increasingly used to demonstrate remotely triggered seismic activity (*e.g.*, West *et al.* 2005; Hill and Prejean 2007; Peng and Chao 2008; Peng *et al.* 2008), it is important to identify such artifacts to avoid false representations. Here we introduced three procedures to remove or reduce such high-frequency artifacts. Each has its own advantage and disadvantage. Applying a high-pass filter to remove the long-period signals that cannot be well resolved by the short time windows prior to computing the spectrogram is the simplest approach. However, the long-period surface waves will not show in the resulting spectrogram. The second approach is to apply multiple bandpass filters to compute the spectrogram. This completely removes the windowing effects in the time domain. However, the multiple bandpass filters may introduce similar windowing effects in the frequency domain, and the resulting spectrogram has relatively low resolution in the frequency axis, due to the finite width of the discrete frequency windows. The third procedure involves the Burg spectrum estimation. It is the most advanced and most computationally expensive approach. It has the best frequency resolution, with some penalties in the precision in the amplitude. In addition, it also introduces certain high-frequency artifacts due to the windowing effect (*e.g.*, Figure 5F, Ⓔ Figure S5F and Ⓔ Figure S6F, available in the electronic supplement to this paper), although they are several orders of magnitudes lower than those from the standard FFT with the Hanning window.

We note that many techniques have been developed in the early 1960–70s to produce frequency-time plots for surface wave analysis (*e.g.*, Kocaoglu and Long 1993 and references therein). We introduced the aforementioned procedures here in this short article, mostly because they can be easily implemented using either MATLAB or SAC's built-in commands. Although there is no perfect solution, these approaches could help to reduce high-frequency artifacts and show the genuine high-frequency signals in the spectrogram plot.

DATA AND RESOURCES

Seismograms used in this study were downloaded from the Northern and Southern California Earthquake Data centers. ◿

ACKNOWLEDGMENTS

REFERENCES

Akaike, H. (1970). Statistical predictor identification. *Annals of the Institute of Statistical Mathematics* **22**, 203–217.

Andersen, N. (1974). On the calculation of filter coefficients for maximum entropy spectral analysis. *Geophysics* **39**, 69; doi:10.1190/1.1440413.

Buttkus, B. (2000). *Spectral Analysis and Filter Theory in Applied Geophysics*. Berlin: Springer.

Burg, J. P. (1967). Maximum entropy spectral analysis. Presented at the 37th Annual International Meeting of Society of Exploration Geophysicists, Oklahoma City, Oklahoma. Reprinted in D. G. Childers, ed. (1978), *Modern Spectrum Analysis*, IEEE Press, 34–41.

Chen, X., and L. T. Long (2000). Spatial distribution of relative scattering coefficients determined from microearthquake coda. *Bulletin of the Seismological Society of America* **90** (2), 512–524.

Delorey, A. A., J. Vidale, J. Steim, and P. Bodin (2008). Broadband sensor nonlinearity during moderate shaking. *Bulletin of the Seismological Society of America* **98**, 1,595–1,601.

Fabian, A., L. Ojha, Z. Peng, and K. Chao (2009). Systematic search of remotely triggered tremor in northern and southern California. *Eos, Transactions, American Geophysical Union* **90** (52), Fall Meeting Supplement, Abstract T13D-1916.

Fischer, A. D., Z. Peng, and C. G. Sammis (2008). Dynamic triggering of high-frequency bursts by strong motions during the 2004 Parkfield earthquake sequence. *Geophysical Research Letters* **35**, L12305; doi:10.1029/2008GL033905.

Gomberg, J., J. L. Rubinstein, Z. Peng, K. C. Creager, and J. E. Vidale (2008). Widespread triggering of non-volcanic tremor in California. *Science* **319**, 173; doi: 10.1126/science.1149164.

Gonzalez-Huizar, H., and A. Velasco (2011). Dynamic triggering: Stress modeling and a case study. *Journal of Geophysical Research* **116**, B02304; doi:10.1029/2009JB007000.

Hellweg, M., R. A. Uhrhammer, S. Ford, and J. Friday (2008). Nonvolcanic tremor in Denali surface waves at broadband stations in northern California: Instrumental causes? *Seismological Research Letters* **79**, 327 (abstract).

Hill, D. P. (2008). Dynamic stresses, coulomb failure, and remote triggering. *Bulletin of the Seismological Society of America* **98** (1), 66–92; doi:10.1785/0120070049.

Hill, D. P. (2010). Surface wave potential for triggering tectonic (non-volcanic) tremor. *Bulletin of the Seismological Society of America* **100** (5A), 1,859–1,878; doi:10.1785/0120090362.

Hill, D. P., and S. G. Prejean (2007). Dynamic triggering, in *Treatise on Geophysics*, ed. G. Schubert, vol. 4, *Earthquake Seismology*, ed. H. Kanamori, 257–292. Amsterdam: Elsevier.

Kocaoglu, A. H., and L. T. Long (1993). A review of time-frequency analysis techniques for estimation of group velocities. *Seismological Research Letters* **64** (2), 157–167.

Peng, Z., and K. Chao (2008). Non-volcanic tremor beneath the Central Range in Taiwan triggered by the 2001 *Mw* 7.8 Kunlun earthquake. *Geophysical Journal International* **175**, 825–829; doi:10.1111/j.1365-246X.2008.03886.x.

Peng, Z., and J. Gomberg (2010). Slow slip phenomena in a global context. *Nature Geoscience* **3**, 599–607; doi:10.1038/ngeo940.

Peng, Z., J. E. Vidale, K. C. Creager, J. L. Rubinstein, J. Gomberg, and P. Bodin (2008). Strong tremor near Parkfield, CA, excited by the 2002 Denali Fault earthquake. *Geophysical Research Letters* **35**, L23305; doi:10.1029/2008GL036080.

Peng, Z., J. E. Vidale, and H. Houston (2006), Anomalous early aftershock decay rates of the 2004 M6 Parkfield earthquake, *Geophysical Research Letters* **33**, L17307, doi:10.1029/2006GL026744.

Peng, Z., J. E. Vidale, A. Wech, R. M. Nadeau, and K. C. Creager (2009). Remote triggering of tremor along the San Andreas fault in central California. *Journal of Geophysical Research* **114**, B00A06; doi:10.1029/2008JB006049.

Prejean, S. G., D. P. Hill, E. E. Brodsky, S. E. Hough, M. J. S. Johnston, S. D. Malone, D. H. Oppenheimer, A. M. Pitt, and K. B. Richards-Dinger (2004). Remotely triggered seismicity on the United States West Coast following the *Mw* 7.9 Denali fault earthquake. *Bulletin of the Seismological Society of America* **94**, S348–S359.

Rubinstein, J. L., J. E. Vidale, J. Gomberg, P. Bodin, K. C. Creager, and S. D. Malone (2007). Non-volcanic tremor driven by large transient shear stresses. *Nature* **448**, 579–582.

Rubinstein, J. L., D. R. Shelly, and W. L. Ellsworth (2010). Non-volcanic tremor: A window into the roots of fault zones, in *New Frontiers in Integrated Solid Earth Sciences*, ed. S. Cloetingh and J. Negendank, 287–314. Dordrecht and New York: Springer.

Ulrych, T. J., and T. N. Bishop (1975). Maximum entropy spectral analysis and autoregressive decomposition. *Reviews of Geophysics* **13** (1), 183–200.

Velasco, A. A., S. Hernandez, T. Parsons, and K. Pankow (2008). Global ubiquity of dynamic earthquake triggering. *Nature Geoscience* **1**, 375–379; doi:10.1038/ngeo204.

West, M., J. J. Sanchez, and S. R. McNutt (2005). Periodically triggered seismicity at Mount Wrangell, Alaska, after the Sumatra earthquake. *Science* **308**, 1,144–1,146; doi:10.1126/science.1112462.

School of Earth and Atmospheric Sciences
The Georgia Institute of Technology
311 Ferst Drive
Atlanta, Georgia 30332-0340 U.S.A.
zpeng@gatech.edu
(Z. P.)